# Supplementary Information for

Urban−rural gradients reveal joint control of elevated $CO_2$ and temperature on extended photosynthetic seasons

Songhan Wang, Weimin Ju, Josep Peñuelas, Alessandro Cescatti, Yuyu Zhou, Yongshuo Fu, Alfredo Huete, Min Liu, Yongguang Zhang
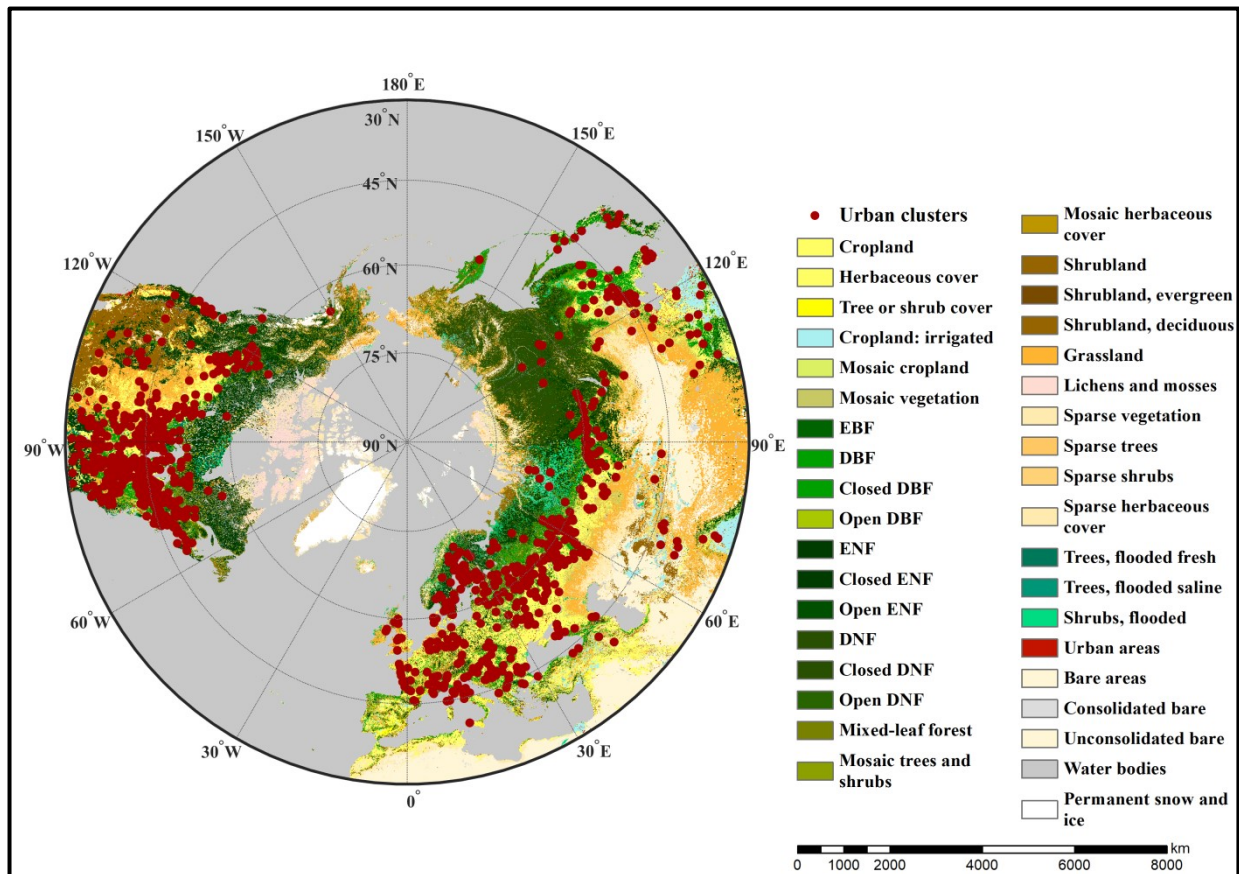
Yongguang Zhang
Email: yongguang_zhang@nju.edu.cn

**This PDF file includes:**

Supplementary Figure 1 to 18
Supplementary Table 1 to 3
References for SI reference citations

**Supplementary Figure 1 | Locations of the study areas and background land-cover types.** Red dots indicate the 880 urban clusters at mid–high latitudes in the Northern Hemisphere (≥30°). The background colours represent the land-cover types extracted from the Climate Change Initiative product for 2015. EBF: evergreen broadleaf forest; DBF: deciduous broadleaf forest; ENF: evergreen needleleaf forest; DNF: deciduous needleleaf forest.
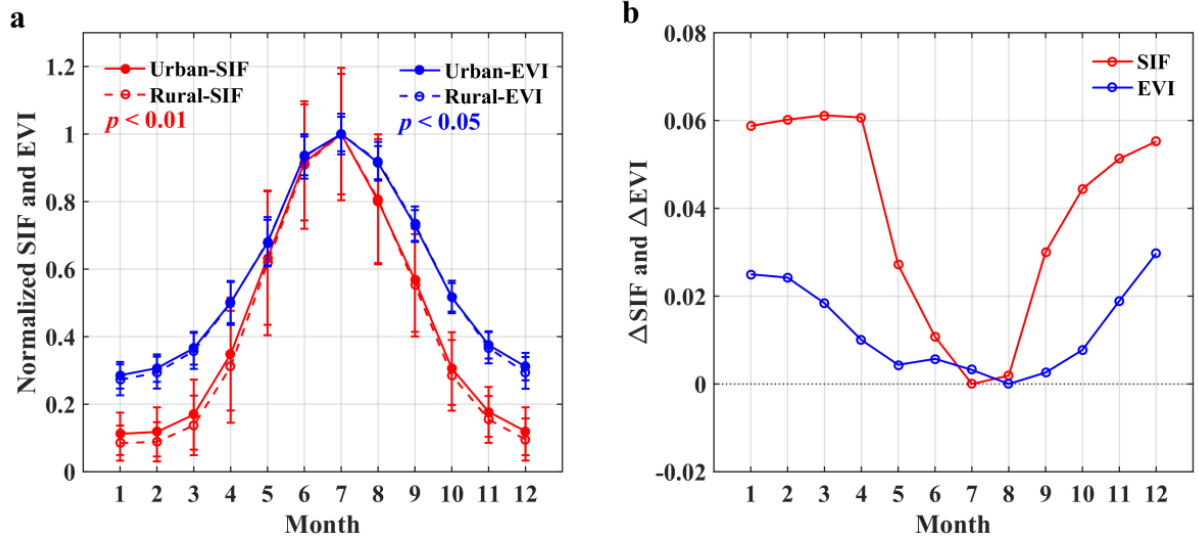
**Supplementary Figure 2 | Seasonal variation of SIF and EVI in urban and rural areas. a**, Normalized monthly EVI and SIF seasonal cycles for urban and rural areas from 2015 to 2017 at mid–high latitudes in the Northern Hemisphere. We chose 30-km rural buffers as the representative area for rural conditions. Error bars indicate monthly standard deviations. $p$ indicates the significance of the difference between urban and rural SIF or EVI (two-sample Kolmogorov–Smirnov test). **b**, Monthly normalized urban–rural $\Delta$SIF and $\Delta$EVI ($\Delta$SIF = $SIF_{urban} - SIF_{rural}$ and $\Delta$EVI = $EVI_{urban} - EVI_{rural}$). The values in urban areas are higher than those in rural areas during spring and autumn for both SIF and EVI. The urban–rural differences of SIF are significantly higher than those of EVI.
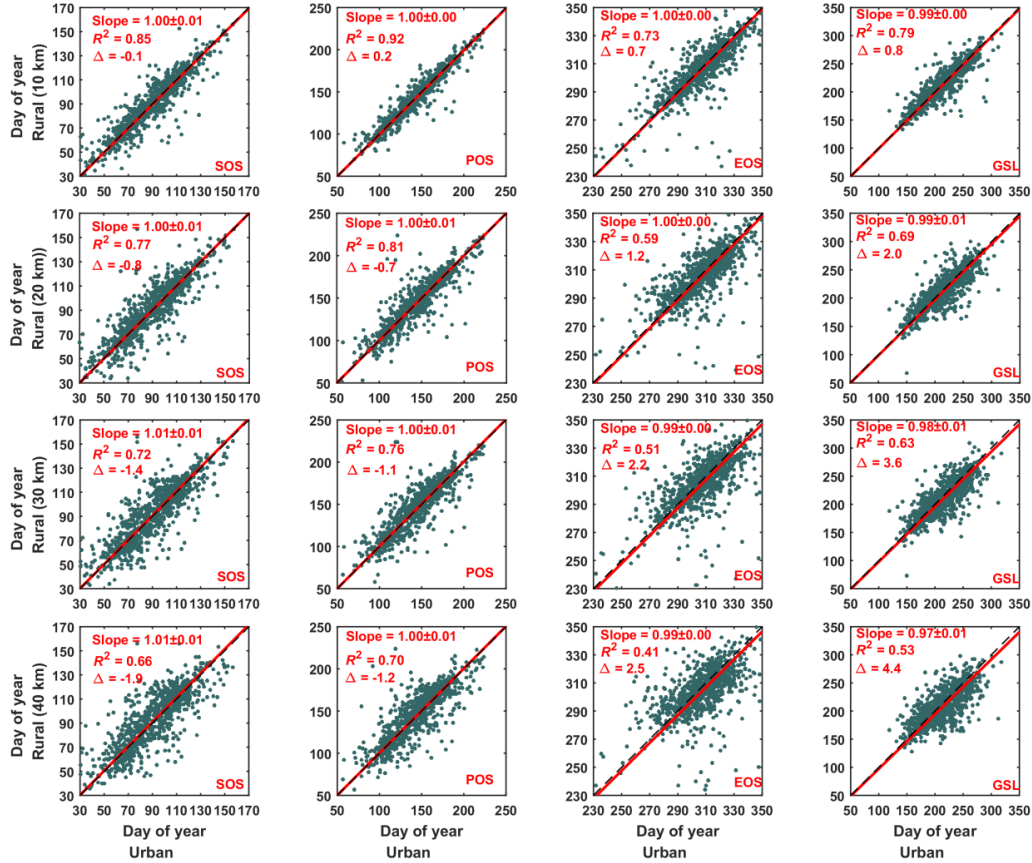
**a** **SIF**
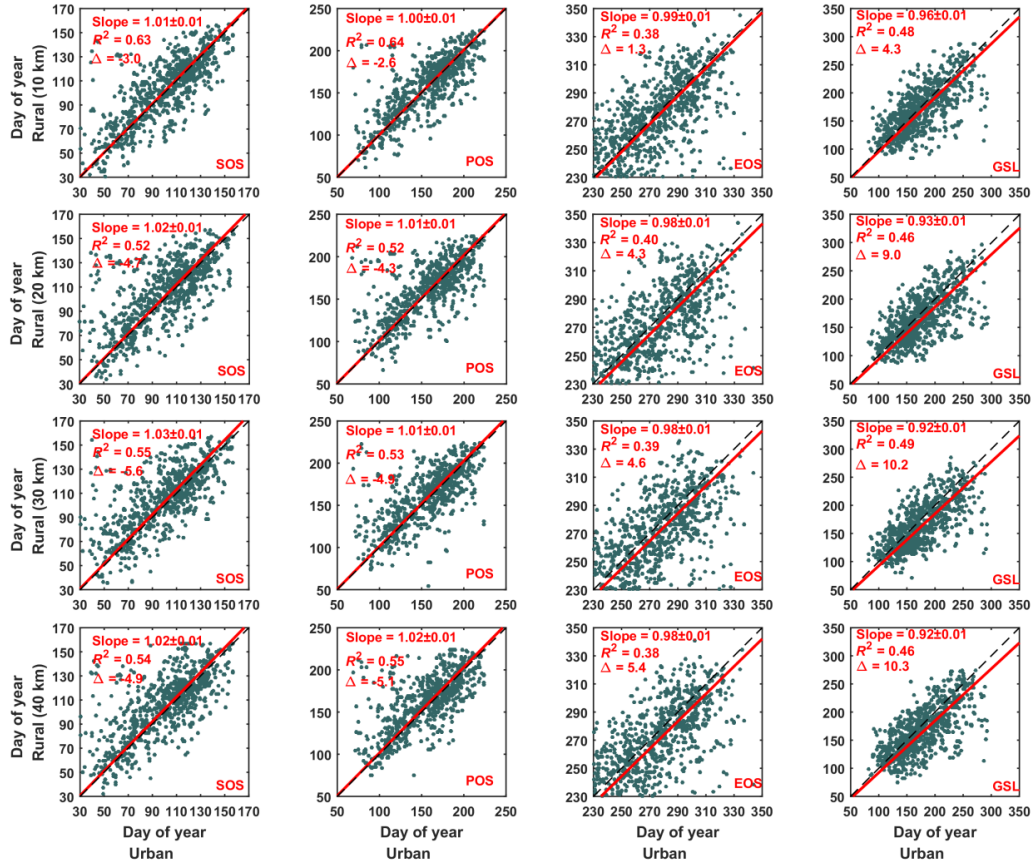
**b** **EVI**

**Supplementary Figure 3 | SIF- and EVI-based phenological indicators (SOS, POS, EOS and GSL) for all urban clusters and their corresponding rural buffers (*n* = 880).** In each plot, the x-axis shows the timings of the relevant phenology indicator in urban areas, and the y-axis shows the timings in the surrounding rural areas (10-40 km buffers, at distances of 10, 20, 30 and 40 km from the relevant corresponding urban area). The columns represent the phenological indicators (SOS: start of growing season; POS: peak of growing season; EOS: end of growing season; GSL: length of growing season). The black dotted lines represent the 1:1 lines, and the solid red lines represent the regression lines between urban and rural phenological indicators. The slopes and 95% confidence intervals of each regression line are shown. Slopes greater than 1 indicate that the phenological stage is occurring at a later date in rural areas than urban areas. Δ represents the mean difference between urban areas and rural buffers. In all cases, *p* < 0.001 (*p* indicates the significance of the linear regression).
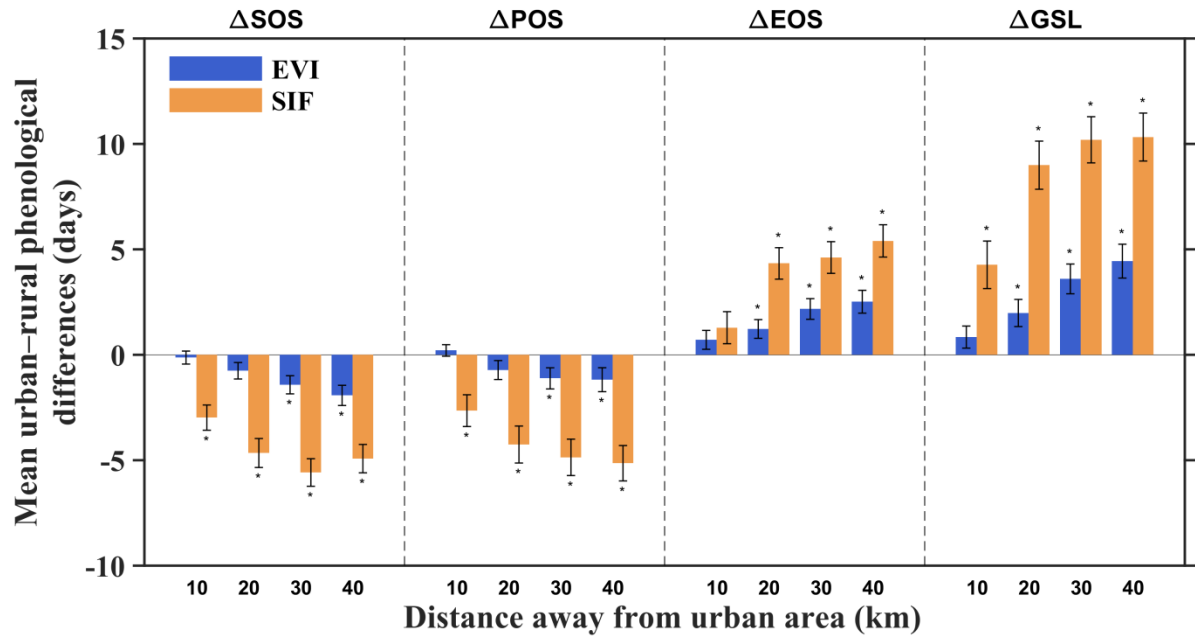
**Supplementary Figure 4 | Mean differences in phenological metrics for SIF and EVI between urban areas and corresponding rural buffer zones of increasing distances from the city.** The operator Δ represents the differences in phenological indicators between urban areas and rural buffers (e.g., ΔSOS = $SOS_{urban} - SOS_{rural}$). Error bars represent standard errors of the mean ($n = 880$); $p$ represents the significance between the mean value and zero; *: $p <$ 0.05. SOS: start of growing season; POS: peak of growing season; EOS: end of growing season; GSL: length of growing season.
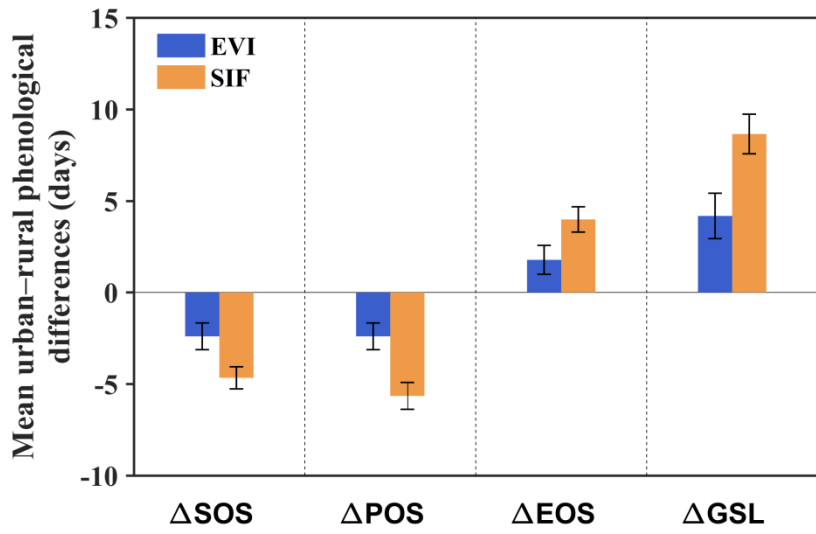
**Supplementary Figure 5 | Mean urban–rural phenological differences based on SIF and EVI, which have the same 5-km spatial resolution.** We firstly resampled the OCO-2 SIF and MODIS EVI to a spatial resolution of 5 km, and next calculated the phenology indicators in urban clusters and corresponding rural buffers following the same procedure in the main text. SOS, start of growing season; POS, peak of growing season; EOS, end of growing season; GSL, length of growing season. The operator $\Delta$ represents the differences in phenological indicators between urban areas and rural buffers (e.g., $\Delta SOS = SOS_{urban} - SOS_{rural}$). The error bars represent standard errors of the mean ($n = 880$).
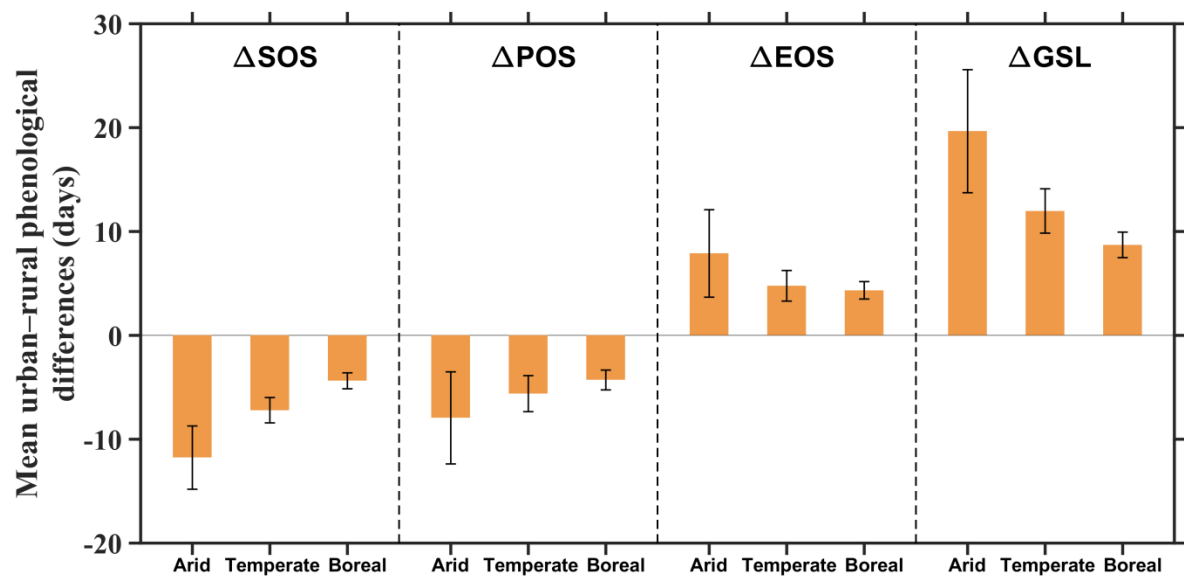
**Supplementary Figure 6 | Mean urban–rural phenological differences (ΔSOS, ΔPOS, ΔEOS and ΔGSL) across different climate zones.** The x-axis represents different climate zones (i.e., arid, temperate and boreal) from the Köppen–Geiger classification zones. The y-axis represents the mean urban–rural phenological differences. Error bars represent standard errors of the mean. SOS: start of growing season; POS: peak of growing season; EOS: end of growing season; GSL: length of growing season.
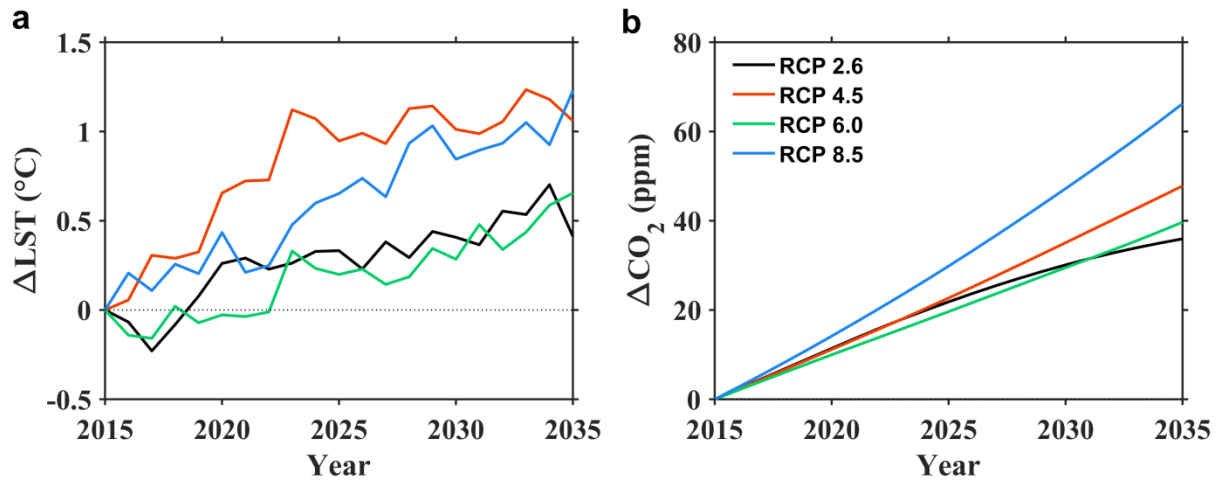
**Supplementary Figure 7 | Land surface temperature (LST) and CO$_2$ concentration changes from 2015 for four projected Representative Concentration Pathway (RCP) scenarios. a**, Mean LST changes from 2015 at mid- to high-latitudes in the Northern Hemisphere (≥30°) simulated by four Earth system models (CSIRO-Mk3.6.0, GFDL-CM3, GISS-E2-H and NorESM1-M) from the Coupled Model Intercomparison Project Phase 5 (CMIP5). **b**, Projected CO$_2$ concentration changes from 2015.
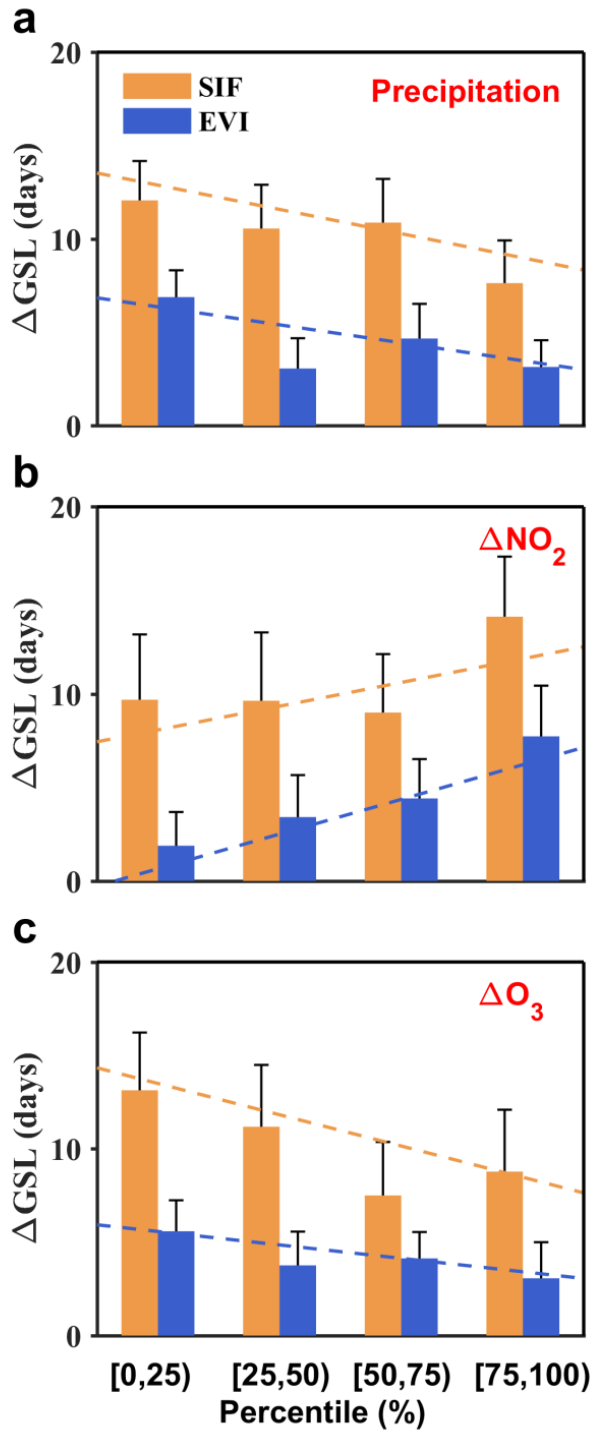
**Supplementary Figure 8 | Urban–rural phenological differences (ΔGSL) across different environmental factors: (a) precipitation; (b) urban–rural NO₂ difference (ΔNO₂); (c) urban–rural O₃ difference (ΔO₃).** Based on precipitation, $\Delta NO_2$ and $\Delta O_3$, the 880 urban clusters are classified into four categories using different quartiles. The mean values and standard errors of the mean are shown with bars and error-bars. The dashed lines represent the linear regression of the mean values. $\Delta NO_2 = NO_{2\,urban} - NO_{2\,rural}$; $\Delta O_3 = O_{3\,urban} - O_{3\,rural}$. GSL: length of growing season.
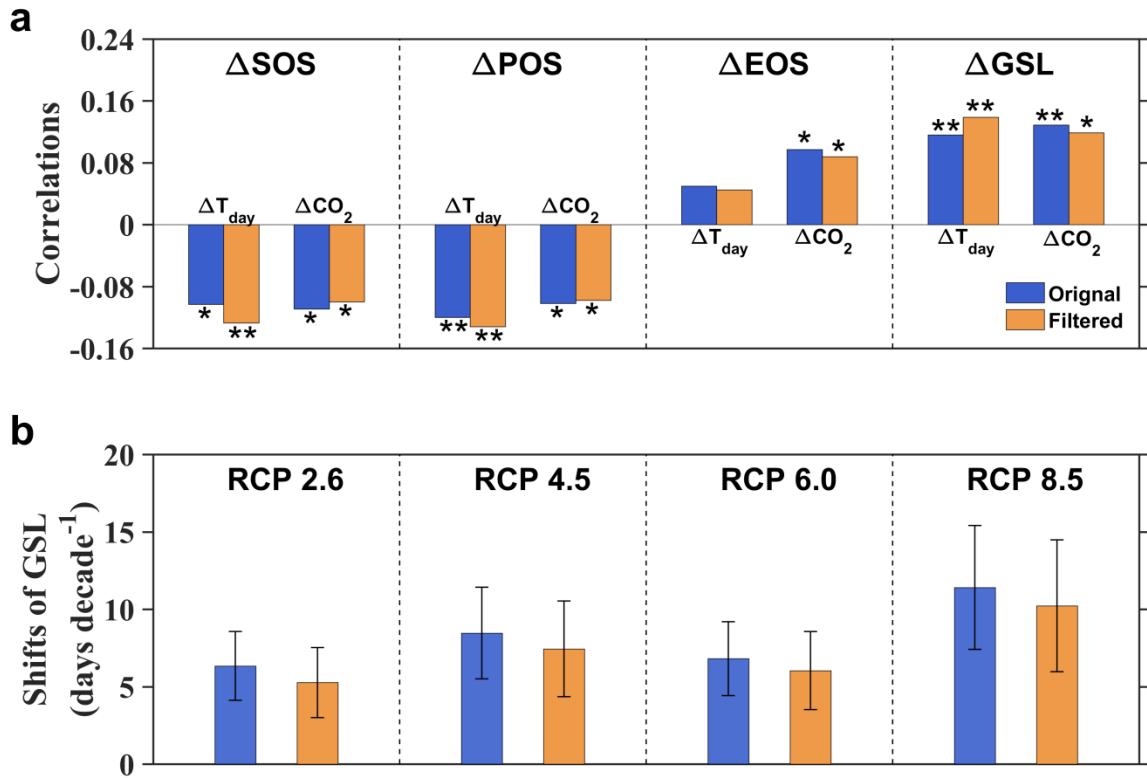
**Supplementary Figure 9 | Results after excluding the urban clusters in arid climate zones**.
**a**, Partial correlations of SIF urban–rural phenological differences (ΔSOS, ΔPOS, ΔEOS and ΔGSL) with $\Delta T_{day}$ and $\Delta CO_2$, based on all the 880 urban clusters ('Original') and the remaining urban clusters after excluding those in the arid climate zones ('Filtered'). $\Delta T_{day}$: daytime urban–rural land surface temperature difference; $\Delta CO_2$: urban–rural $CO_2$ difference. SOS: start of growing season; POS: peak of growing season; EOS: end of growing season; GSL: length of growing season. *: $p < 0.05$; **: $p < 0.01$. **b**, Projected shifts of GSL in per decade (days·decade$^{-1}$). The error bars represent standard errors of the mean.
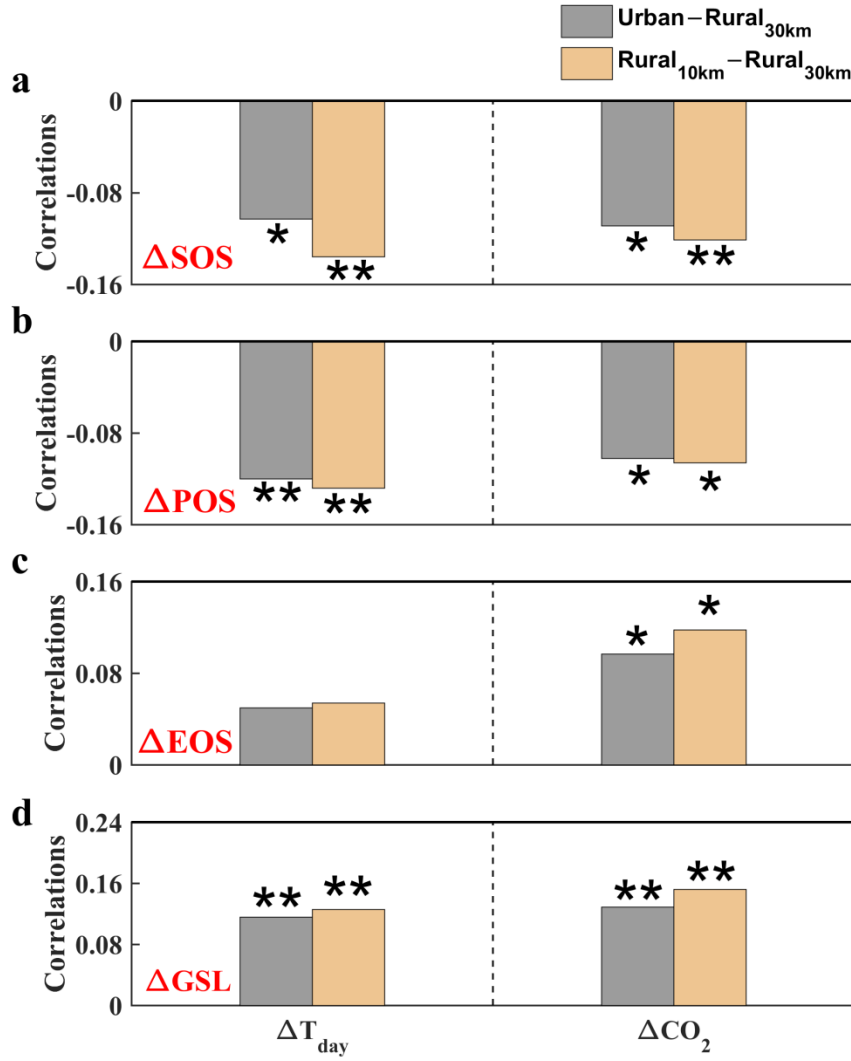
**Supplementary Figure 10 | Partial correlations of SIF urban–rural$_{30km}$ and rural$_{10km}$–rural$_{30km}$ phenological differences with $\Delta T_{day}$ and $\Delta CO_2$.** Urban, rural$_{10km}$ and rural$_{30km}$ represent the phenology indicators in the urban clusters, 10-km rural buffers and 30-km rural buffers, respectively. $\Delta T_{day}$: daytime urban–rural land surface temperature difference; $\Delta CO_2$: urban–rural $CO_2$ difference. SOS: start of growing season; POS: peak of growing season; EOS: end of growing season; GSL: length of growing season. *: $p < 0.05$; **: $p < 0.01$ ($n = 880$).
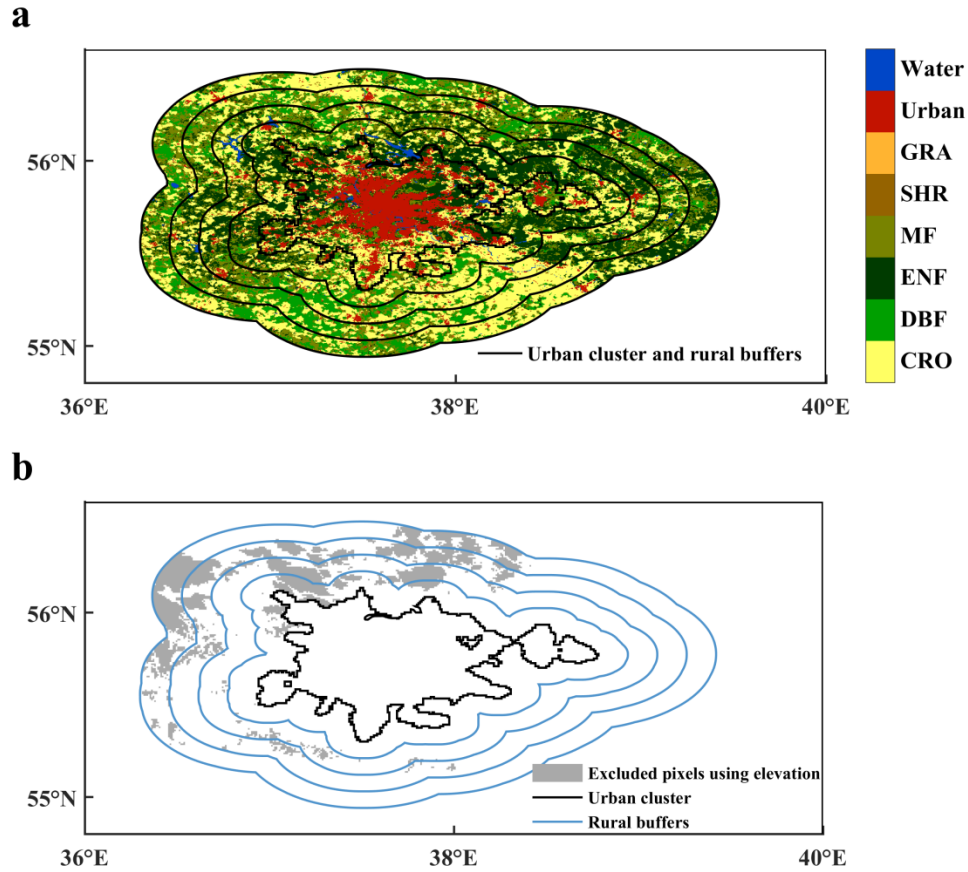
**Supplementary Figure 11 | An example of the urban cluster and its corresponding rural buffers using Moscow**. **a,** The urban cluster and rural buffers (10-, 20-, 30- and 40- km) and the background land cover classifications. The urban cluster was derived from the satellite nighttime light data using a cluster-based method, which defined the boundary between urban and rural areas, regardless of the internal spatial heterogeneity. The rural buffers were defined by extending 10, 20, 30 and 40 km outward from the urban cluster perimeter. We excluded the pixels that were water bodies or crops in this analysis. **b,** The pixels excluded using the elevation mask. We also excluded the pixels in the rural areas which had elevations greater than ±50 m of the average elevation of urban pixels.
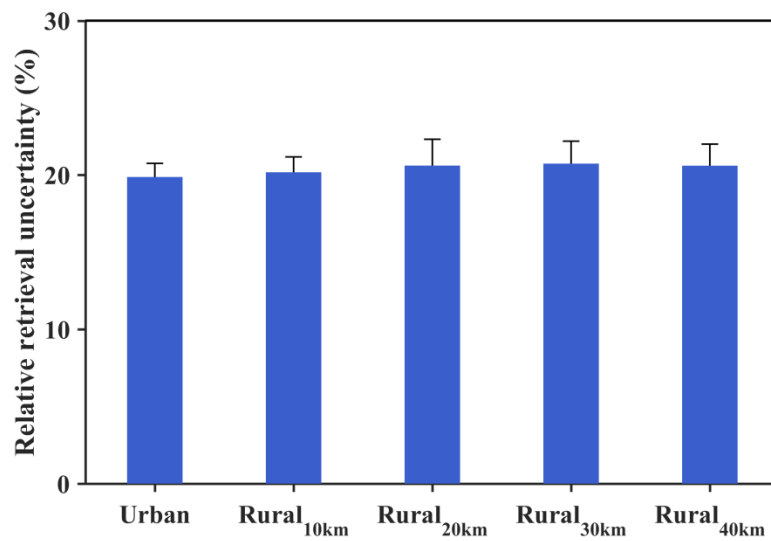
**Supplementary Figure 12 | Relative retrieval uncertainties of single SIF measurements in urban clusters and corresponding rural buffers**. The relative retrieval uncertainties were calculated as the ratios between single-measurement precision and the absolute SIF values, which were derived from the original OCO-2 SIF products. The mean values and standard errors (SEs) of the mean are shown with bars and error-bars.
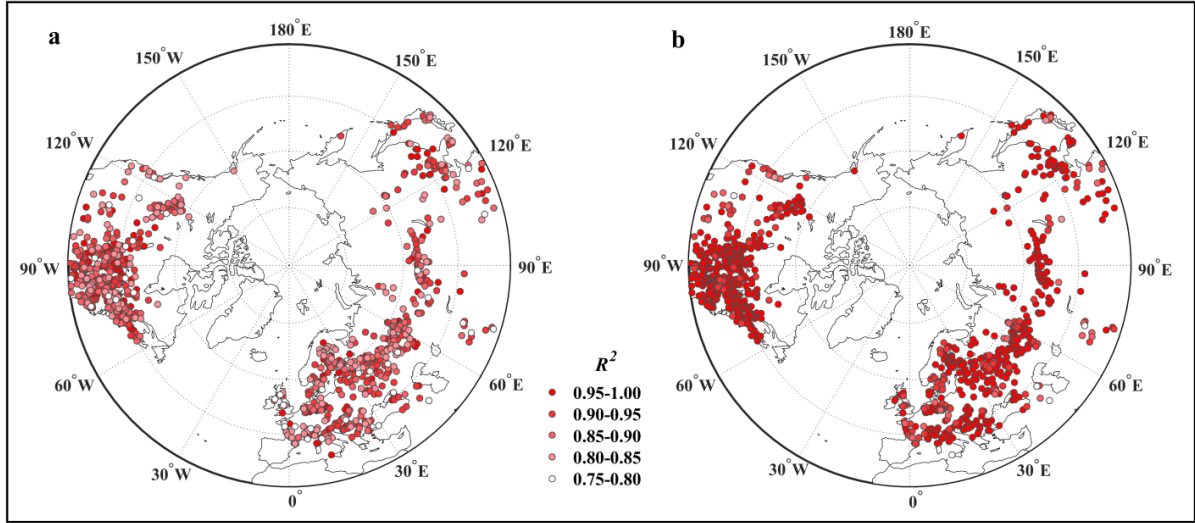
**Supplementary Figure 13 | $R^2$ values between the observation time series and double-sigmoidal fits for SIF (a) and EVI (b).** Most of the $R^2$ values for SIF are greater than 0.8. Only a few urban clusters have $R^2$ values between 0.75 and 0.8. Most of the $R^2$ values for EVI are greater than 0.9, which are higher than those for SIF.
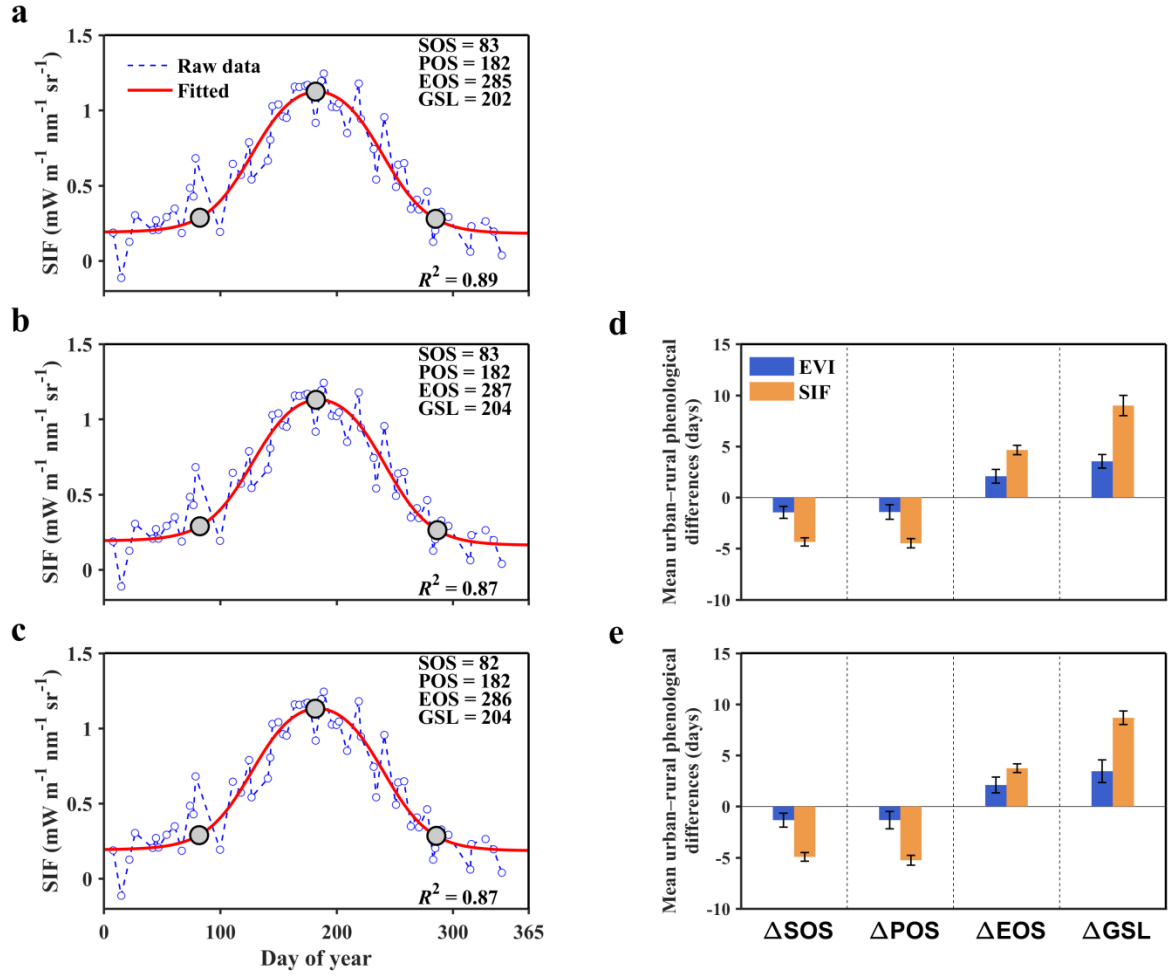
**Supplementary Figure 14 | Robustness of the phenology extraction method. a,** An example of the extraction of the phenological indicators. The gray points represent the SOS, POS and EOS respectively. SOS, start of growing season; POS, peak of growing season; EOS, end of growing season; GSL, length of growing season. **b,** Extraction of the phenological indicators by changing the moving window, i.e., we assigned a weight of two if a central point was within ±50% of the median for a moving window of five points. **c,** Extraction of the phenological indicators without using the weighting scheme. **d,** Similar with Fig. 1 in the main text, except the results were calculated by setting the moving window to five points. The operator $\Delta$ represents the differences in phenological indicators between urban areas and rural buffers (e.g., $\Delta$SOS = $SOS_{urban} - SOS_{rural}$). The error bars represent standard errors of the mean ($n$ = 880). **e,** Similar with Fig. 1 in the main text, except the results were calculated without using the weighting scheme.
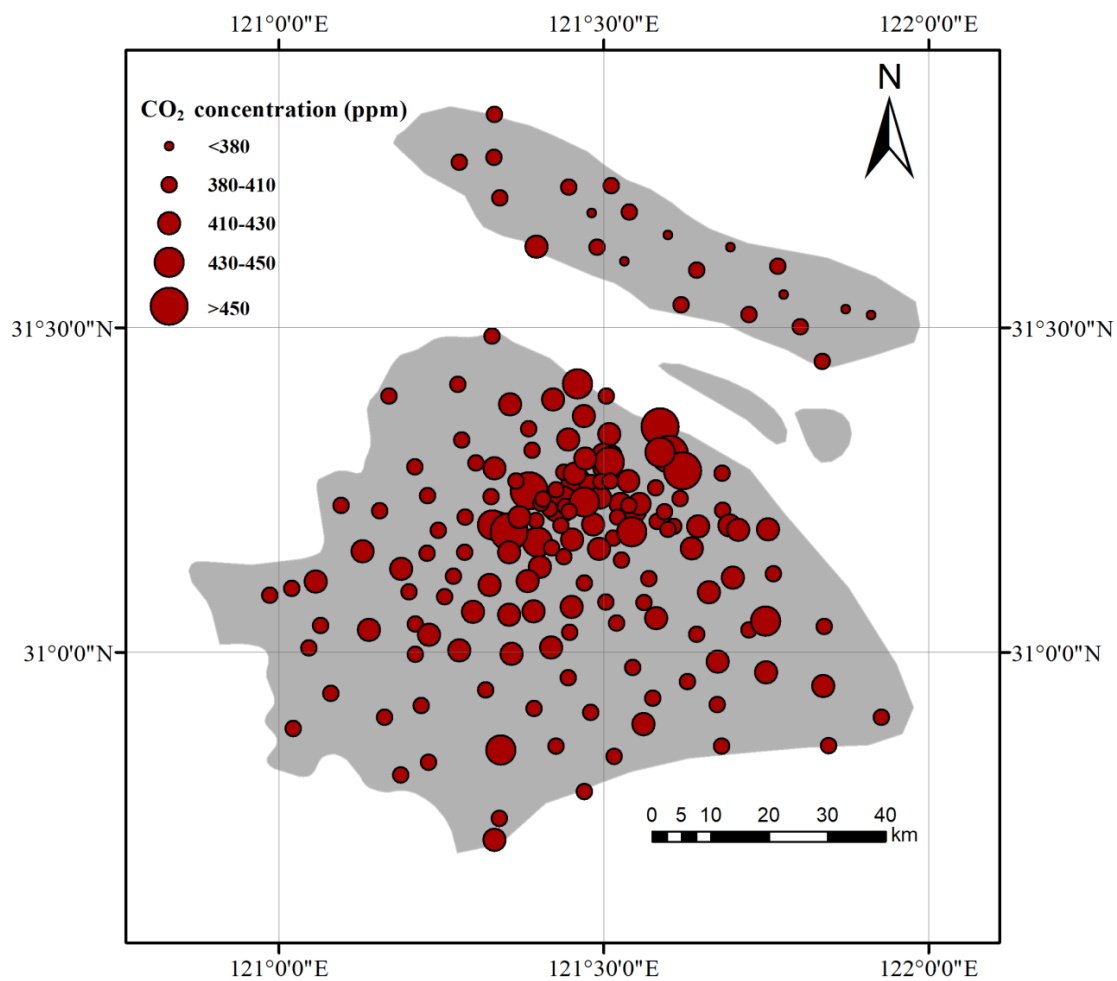
**Supplementary Figure 15 | Spatial distribution of near-surface CO₂ concentrations in Shanghai from 172 sampling points.**
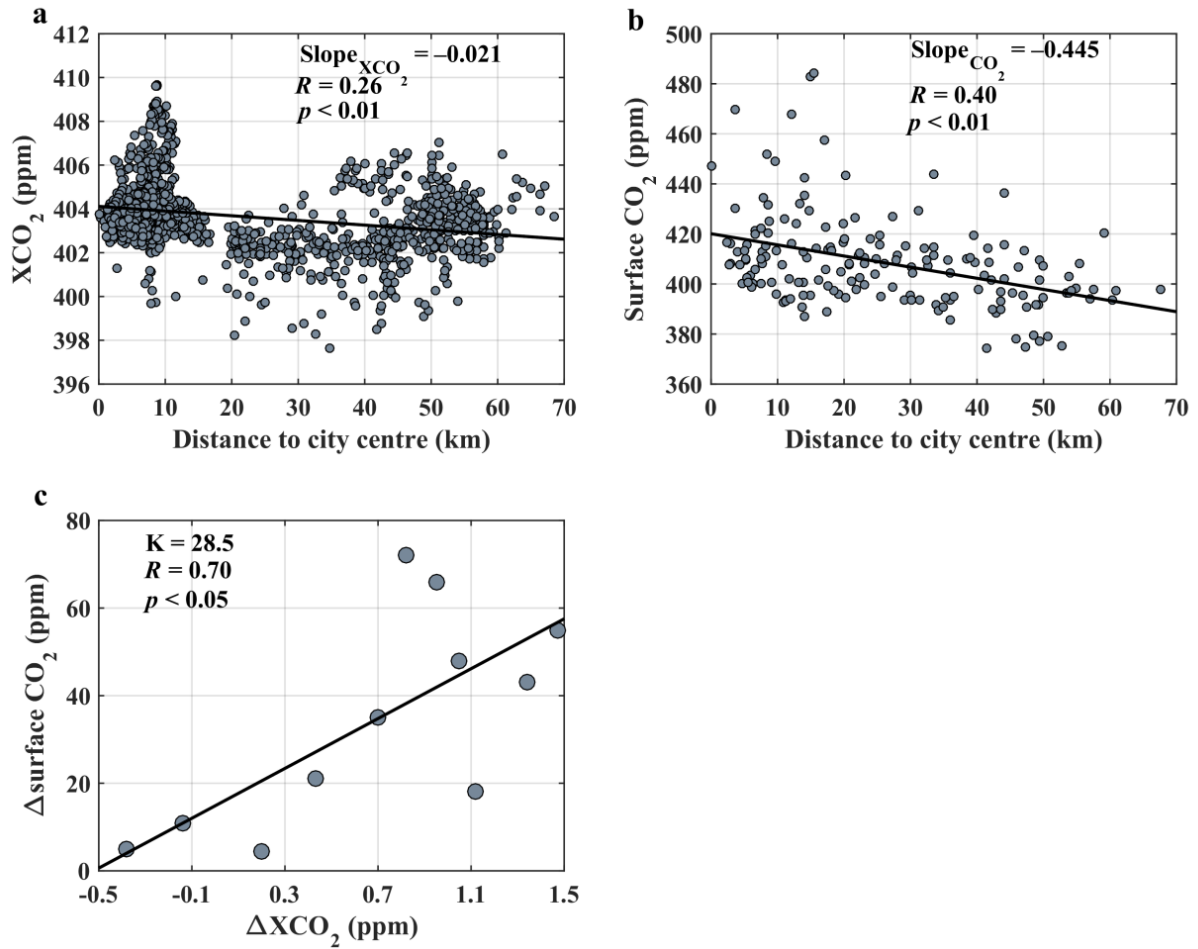
**Supplementary Figure 16 | Factors for converting urban–rural XCO$_2$ gradients into surface CO$_2$ gradients. a**, Atmospheric XCO$_2$ observations across Shanghai as a function of the distance to the city centre. **b**, Surface CO$_2$ measurements in Shanghai as a function of the distance to the city centre. The factor for converting XCO$_2$ gradients into surface CO$_2$ gradients (K) is Slope$_{CO2}$/Slope$_{XCO2}$ = 21.2. **c**, Scatter plots between urban–rural observed XCO$_2$ gradients and surface CO$_2$ gradients from previous studies, with K = 28.5.
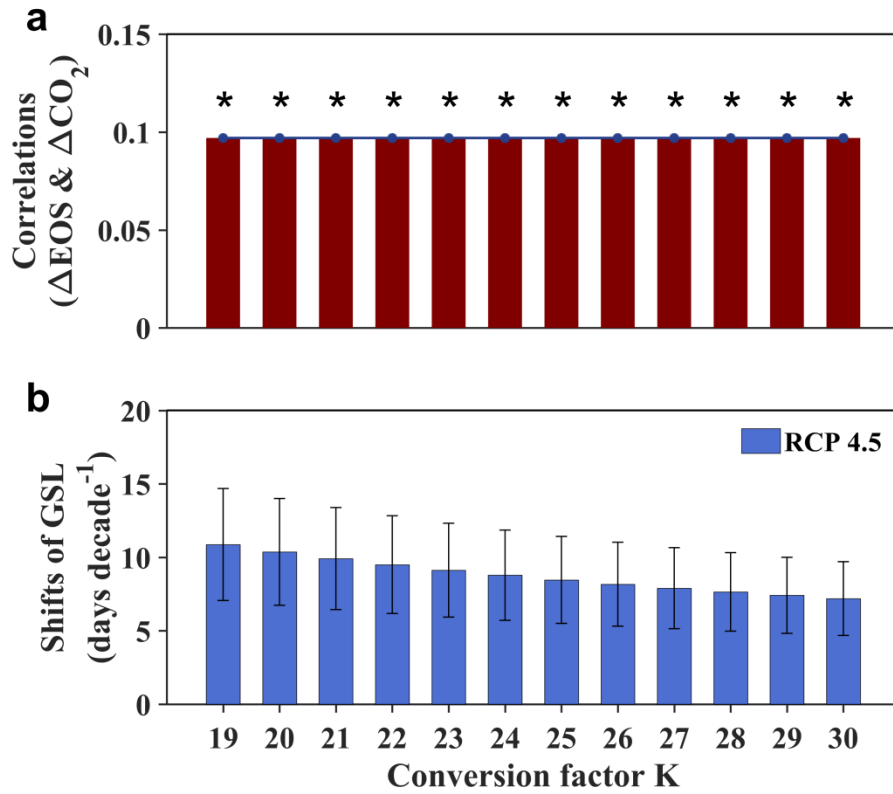
**Supplementary Figure 17 | Partial correlations of urban–rural EOS gradients with $CO_2$ gradients (a) and predicted GSL shifts based on RCP 4.5 scenario (b) using different K values.** K represents the factor for converting $XCO_2$ gradients into surface $CO_2$ gradients. The K factor derived from the first approach was $21.2 \pm 8.3$; while that from the second approach was $28.5 \pm 9.5$ (mean ± standard error). Therefore we used a series of K factors ranging from 19 to 30, which was the intersection of the K factors estimated from these two approaches. $\Delta CO_2$: urban–rural $CO_2$ difference. EOS: end of growing season; GSL: length of growing season. *: $p < 0.05$ ($n = 880$). The error bars in panel b represent the standard errors (SEs) of the mean.
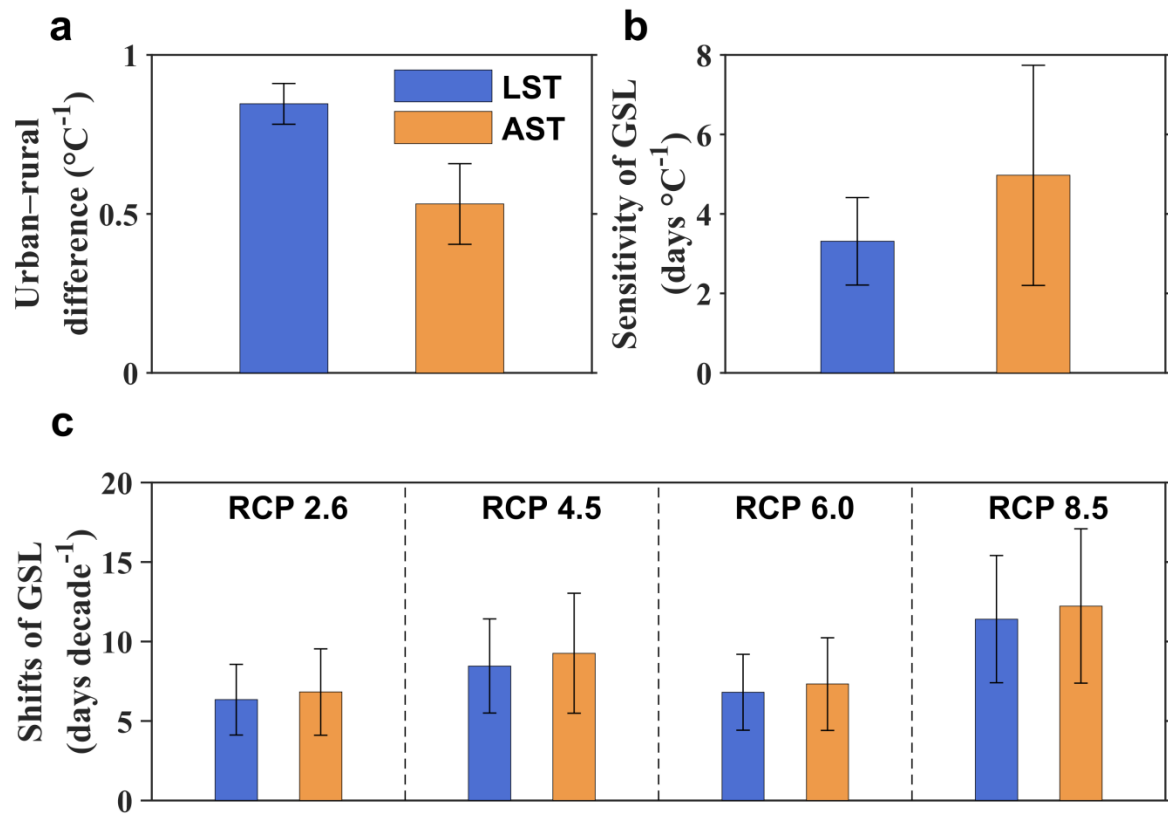
**Supplementary Figure 18 | Comparisons of the future GSL (length of growing season) shifts based on urban–rural land surface temperature (LST) gradients and air surface temperature (AST) gradients. a**, Mean urban–rural LST difference and AST difference. **b**, sensitivities of GSL to LST and AST. **c**, Projected shifts of GSL in per decade (days·decade⁻¹) based on urban–rural LST differences and AST differences, respectively. The error bars represent standard errors of the mean.

**Supplementary Table 1 | Descriptions of the data sets.**

| Variable | Origin | Temporal resolution | Spatial resolution | Date | Reference |
|---|---|---|---|---|---|
| Urban clusters | – | – | 1 km | 2013 | Zhou, et al. [1] |
| SIF (solar-induced chlorophyll fluorescence) | OCO-2 (version 8r) | Approximately 16 days | $1.3 \times 2.25$ $km^2$ | 2015–2017 | Frankenberg, et al. [2] |
| EVI (enhanced vegetation index) | MODIS (MYD13A2) | 16 days | 1 km | 2015–2017 | Huete, et al. [3] |
| LST (land surface temperature) | MODIS (MYD11A2) | 16 days | 1 km | 2015–2017 | Wan and Dozier [4] |
| $XCO_2$ (column-averaged $CO_2$ mixing ratios) | OCO-2 (version 8r) | approximately 16 days | $1.3 \times 2.25$ $km^2$ | 2015–2017 | Crisp, et al. [5] |
| Air temperature | GHCN-CAMS analyzed data | monthly | 0.5° | 2015–2017 | Fan and Van den Dool [6] |
| Precipitation | GPM-IMERG data | monthly | 0.1° | 2015–2017 | Huffman, et al. [7] |
| Land cover | ESA CCI projects | – | 300 m | 2015 | ESA [8] |
| Altitude | GTOPO30 DEM | – | 1 km | 1996 | Gesch, et al. [9] |
| AST (air surface temperature) | TerraClimate | monthly | 4 km | 2015–2017 | Abatzoglou, et al. [10] |
| $NO_2$ | Ozone Monitoring Instrument (OMI) | monthly | 0.125° | 2015–2017 | Boersma, et al. [11] |
| $O_3$ | Ozone Monitoring Instrument (OMI) | monthly | 0.25° | 2015–2017 | Veefkind, et al. [12] |

**Supplementary Table 2 | Observations of urban–rural surface CO₂ gradients from previous studies.** The urban–rural gradient for Phoenix ranges from 19 to 185 ppm, which is highly variable. Thus, we excluded these observations when calculating the conversion factor. The urban–rural gradients from these studies averaged approximately 30 ppm (excluding the Phoenix data).

| No. | City, country | Year | Observation method | Urban $CO_2$ concentration (ppm) | Rural $CO_2$ concentration (ppm) | Urban–rural $CO_2$ gradient (ppm) | Relative $CO_2$ increase (%) | Reference |
|---|---|---|---|---|---|---|---|---|
| 1 | Phoenix, USA | 1998 | Mobile measurements | 555 | 370 | 185 | 50.0 | Idso, et al. [13] |
| 2 | Phoenix, USA | 2000 | Mobile measurements | 619.3(max) | 424.3–490.6 | – | 41.5 | Idso, et al. [14] |
| 3 | Phoenix, USA | 2002 | Site observations | 396 | 377 | 19 | 5.0 | Day, et al. [15] |
| 4 | Essen, Germany | 2002–2003 | Mobile measurements | 404 | 371 | 33 | 8.9 | Henninger and Kuttler [16] |
| 5 | Essen, Germany | 2010 | Site observations | 417 | 381 | 36 | 9.4 | Büns and Kuttler [17] |
| 6 | Rome, Italy | 1995–2004 | Different zones | 477 | 405 | 72 | 17.8 | Gratani and Varone [18] |
| 7 | Baltimore, USA | 2007 | Site observations | 488 | 422 | 66 | 15.6 | George, et al. [19] |
| 8 | Valladolid, Spain | 2006–2007 | Site observations | 397.8 | 393.3 | 4.5 | 1.1 | García, et al. [20] |
| 9 | Portland, USA | 2009 | Site observations | 408 | 403 | 5 | 1.2 | Rice and Bostrom [21] |
| 10 | Boston, USA | 2011 | Site observations | 414 | 393 | 21 | 5.3 | Briber, et al. [22] |
| 11 | Basel, Switzerland | 2005–2015 | Site observations | – | – | 10.5–12 | – | Schmutz, et al. [23] |
| 12 | Berkeley, USA | 2013 | Site observations | 425 | 407 | 18 | 4.4 | Shusterman, et al. [24] |
| 13 | Nanjing, China | 2008 | Mobile measurements | 435 | 387 | 48 | 12.4 | Zhao, et al. [25] |
| 14 | Xiamen, China | 2011 | Mobile measurements | 477.3 | 434.1 | 43.2 | 10.0 | Li, et al. [26] |
| 15 | Shanghai, China | 2014 | Mobile measurements | 469.2 | 414.1 | 55.1 | 13.3 | Zhu, et al. [27] |

**Supplementary Table 3 | Urban–rural photosynthetic phenological differences (SIF) and explanatory variables based on forward stepwise regression models.** SOS: start of season; POS: peak of season; EOS: end of season; GSL: length of season; $\Delta LST_{day}$: daytime urban–rural land surface temperature difference; $\Delta CO_2$: urban–rural $CO_2$ difference; SE: standard error.

| SIF | Model | Explanatory variables | Coefficient (±SE) | $R^2$ | $p$ |
|---|---|---|---|---|---|
| $\Delta$SOS | 1 | $\Delta LST_{day}$ (°C) | $-1.54 \pm 0.60$ | 0.11 | 0.008 |
| | 2 | $\Delta LST_{day}$ (°C) | $-1.55 \pm 0.60$ | 0.15 | 0.004 |
| | | $\Delta CO_2$ (ppm) | $-0.15 \pm 0.07$ | | |
| $\Delta$POS | 1 | $\Delta LST_{day}$ (°C) | $-2.10 \pm 0.79$ | 0.12 | 0.008 |
| | 2 | $\Delta LST_{day}$ (°C) | $-2.11 \pm 0.78$ | 0.15 | 0.004 |
| | | $\Delta CO_2$ (ppm) | $-0.18 \pm 0.09$ | | |
| $\Delta$EOS | 1 | $\Delta CO_2$ (ppm) | $0.17 \pm 0.07$ | 0.10 | 0.023 |
| $\Delta$GSL | 1 | $\Delta LST_{day}$ (°C) | $3.33 \pm 1.11$ | 0.13 | 0.003 |
| | 2 | $\Delta LST_{day}$ (°C) | $3.31 \pm 1.10$ | 0.19 | 0.000 |
| | | $\Delta CO_2$ (ppm) | $0.32 \pm 0.11$ | | |

# References

1       Zhou, Y. *et al.* A global map of urban extent from nightlights. *Environmental Research Letters* **10**, 054011 (2015).

2       Frankenberg, C. *et al.* Prospects for chlorophyll fluorescence remote sensing from the Orbiting Carbon Observatory-2. *Remote Sensing of Environment* **147**, 1-12 (2014).

3       Huete, A. *et al.* Overview of the radiometric and biophysical performance of the MODIS vegetation indices. *Remote sensing of environment* **83**, 195-213 (2002).

4       Wan, Z. & Dozier, J. A generalized split-window algorithm for retrieving land-surface temperature from space. *IEEE Transactions on geoscience and remote sensing* **34**, 892-905 (1996).

5       Crisp, D. *et al.* The on-orbit performance of the Orbiting Carbon Observatory-2 (OCO-2) instrument and its radiometrically calibrated products. *Atmospheric Measurement Techniques* **10**, 59 (2017).

6       Fan, Y. & Van den Dool, H. A global monthly land surface air temperature analysis for 1948–present. *Journal of Geophysical Research: Atmospheres* **113** (2008).

7       Huffman, G. J. *et al.* NASA global precipitation measurement (GPM) integrated multi-satellite retrievals for GPM (IMERG). *Algorithm theoretical basis document, version* **4**, 30 (2015).

8       ESA. Land Cover CCI Product User Guide Version 2.0.    (2017).

9       Gesch, D. B., Verdin, K. L. & Greenlee, S. K. New land surface digital elevation model covers the Earth. *EOS, Transactions American Geophysical Union* **80**, 69-70 (1999).

10      Abatzoglou, J. T., Dobrowski, S. Z., Parks, S. A. & Hegewisch, K. C. TerraClimate, a high-resolution global dataset of monthly climate and climatic water balance from 1958–2015. *Scientific data* **5**, 170191 (2018).

11      Boersma, K. *et al.* Near-real time retrieval of tropospheric $NO_2$ from OMI. *Atmospheric Chemistry and Physics* **7**, 2103-2118 (2007).

12      Veefkind, J. P., de Haan, J. F., Brinksma, E. J., Kroon, M. & Levelt, P. F. Total ozone from the Ozone Monitoring Instrument (OMI) using the DOAS technique. *IEEE Transactions on Geoscience and Remote Sensing* **44**, 1239-1244 (2006).

13      Idso, C. D., Idso, S. B. & Balling Jr, R. C. The urban $CO_2$ dome of Phoenix, Arizona. *Physical Geography* **19**, 95-108 (1998).

14      Idso, C. D., Idso, S. B. & Balling Jr, R. C. An intensive two-week study of an urban $CO_2$ dome in Phoenix, Arizona, USA. *Atmospheric Environment* **35**, 995-1000 (2001).

15      Day, T. A., Gober, P., Xiong, F. S. & Wentz, E. A. Temporal patterns in near-surface $CO_2$ concentrations over contrasting vegetation types in the Phoenix metropolitan area. *Agricultural and Forest Meteorology* **110**, 229-245 (2002).

16      Henninger, S. & Kuttler, W. Near surface carbon dioxide within the urban area of Essen, Germany. *Physics and Chemistry of the Earth, Parts A/B/C* **35**, 76-84 (2010).

17      Büns, C. & Kuttler, W. Path-integrated measurements of carbon dioxide in the urban canopy layer. *Atmospheric environment* **46**, 237-247 (2012).

18      Gratani, L. & Varone, L. Daily and seasonal variation of $CO_2$ in the city of Rome in relationship with the traffic volume. *Atmospheric Environment* **39**, 2619-2624 (2005).

19      George, K., Ziska, L. H., Bunce, J. A. & Quebedeaux, B. Elevated atmospheric $CO_2$ concentration

and temperature across an urban–rural transect. *Atmospheric Environment* **41**, 7654-7665 (2007).

20      García, M. Á., Sánchez, M. L. & Pérez, I. A. Differences between carbon dioxide levels over suburban and rural sites in Northern Spain. *Environmental Science and Pollution Research* **19**, 432-439 (2012).

21      Rice, A. & Bostrom, G. Measurements of carbon dioxide in an Oregon metropolitan region. *Atmospheric Environment* **45**, 1138-1144 (2011).

22      Briber, B. M., Hutyra, L. R., Dunn, A. L., Raciti, S. M. & Munger, J. W. Variations in atmospheric $CO_2$ mixing ratios across a Boston, MA urban to rural gradient. *Land* **2**, 304-327 (2013).

23      Schmutz, M., Vogt, R. & Parlow, E. in *9th International Conference on Urban Climate*      101-105 (Toulouse, France, 2015).

24      Shusterman, A. A. *et al.* The BErkeley Atmospheric $CO_2$ Observation Network: initial evaluation. *Atmospheric Chemistry and Physics* **16**, 13449-13463 (2016).

25      Zhao, H., Ouyang, y. & Qi, j. Near-surface atmospheric properties along an urban center-suburban-urban forest gradient in summer in Nanjing City. *ACTA ECOLOGICA SINICA* **29**, 6654-6663 (2009).

26      Li, Y., Xing, Z. & Mu, C. Spatial and Temporal Variations of Near Surface Atmospheric $CO_2$ with Mobile Measurements in Fall and Spring in Xiamen, China. *ENVIRONMENT SCIENCE* **35**, 1671-1679 (2014).

27      Zhu, X., Pan, C. & Liu, M. Spatial characristics of near surface $CO_2$ concentrations and analysis of its influencing factors in spring in Shanghai city. *Resources and Environment in the Yangtze Basin* **24** (2015).